ADVANCED FUNCTIONAL MATERIALS
www.afm-journal.de

Phase-Dependent Band Gap Engineering in Alloys of Metal-Semiconductor Transition Metal Dichalcogenides

Shuxi Wang, John Cavin, Zahra Hemmat, Khagesh Kumar, Alexander Ruckel, Leily Majidi, Hamed Gholivand, Radwa Dawood, Jordi Cabana, Nathan Guisinger, Robert F. Klie, Fatemeh Khalili-Araghi, Rohan Mishra, and Amin Salehi-Khojin**

Bandgap engineering plays a critical role in optimizing the electrical, optical and (photo)-electrochemical applications of semiconductors. Alloying has been a historically successful way of tuning bandgaps by making solid solutions of two isovalent semiconductors. In this work, a novel form of bandgap engineering involving alloying non-isovalent cations in a 2D transition metal dichalcogenide (TMDC) is presented. By alloying semiconducting $MoSe_2$ with metallic $NbSe_2$, two structural phases of $Mo_{0.5}Nb_{0.5}Se_2$, the *1T* and *2H* phases, are produced each with emergent electronic structure. At room temperature, it is observed that the *1T* and *2H* phases are semiconducting and metallic, respectively. For the *1T* structure, scanning tunneling microscopy/spectroscopy (STM/STS) is used to measure band gaps in the range of 0.42–0.58 at 77 K. Electron diffraction patterns of the *1T* structure obtained at room temperature show the presence of a nearly commensurate charge density wave (NCCDW) phase with periodic lattice distortions that result in an uncommon 4 × 4 supercell, rotated approximately 4° from the lattice. Density-functional-theory calculations confirm that local distortions, such as those in a NCCDW, can open up a band gap in *1T*-$Mo_{0.5}Nb_{0.5}Se_2$, but not in the *2H* phase. This work expands the boundaries of alloy-based bandgap engineering by introducing a novel technique that facilitates CDW phases through alloying.

1. Introduction

Due to their diverse chemical compositions and structural phases, 2D TMDCs are strong candidates for bandgap engineering. Thus far, several methods have been studied to tune bandgaps in semiconductor TMDCs including reducing dimensionality,[1] creating inter- and intra-heterostructures,[2–4] introducing internal strain,[5] and alloying.[6–9] Among these methods, alloying is a scalable, cost-effective and controllable approach which has already been carried out using different synthesis techniques.[8,10,11] As long as two semiconductors share similar lattice parameters and have isovalent alloyed atoms, a continuous spectrum of bandgap values are accessible.[6,12] The relationship between the bandgap and the alloying concentration is typically close to a linear interpolation with a small bowing parameter. The case for non-isovalent alloys can be quite different. A simple example is the alloying of a metal and a semiconductor: an electron counting argument suggests that sufficient addition of metal into the semiconductor will raise the Fermi level into the unoccupied conduction band, turning it into a metal. This behavior is clearly not continuous or useful for bandgap engineering. In this work, we present an example of alloying a semiconductor and a metal to form a semiconductor through phase-dependent bandgap engineering.[13]

S. Wang, A. Ruckel, R. Dawood, Prof. R. F. Klie, Prof. F. Khalili-Araghi
Department of Physics
University of Illinois at Chicago
Chicago, IL 60607, USA

J. Cavin
Department of Physics
Washington University in St. Louis
St. Louis, MO 63130, USA

Z. Hemmat, L. Majidi, H. Gholivand, Prof. A. Salehi-Khojin
Department of Mechanical and Industrial Engineering
University of Illinois at Chicago
Chicago, IL 60607, USA
E-mail: salehikh@uic.edu

The ORCID identification number(s) for the author(s) of this article can be found under https://doi.org/10.1002/adfm.202004912.

DOI: 10.1002/adfm.202004912

K. Kumar, Prof. J. Cabana
Department of Chemistry
University of Illinois at Chicago
Chicago, IL 60607, USA

Dr. N. Guisinger
Center for Nanoscale Materials
Argonne National Laboratory
Argonne, IL 60439, USA

Prof. R. Mishra
Department of Mechanical Engineering and Material Science
Washington University in St. Louis
St. Louis, MO 63130, USA
E-mail: rmishra@wustl.edu

Prof. R. Mishra
Institute of Materials Science and Engineering
Washington University in St. Louis
St. Louis, MO 63130, USA

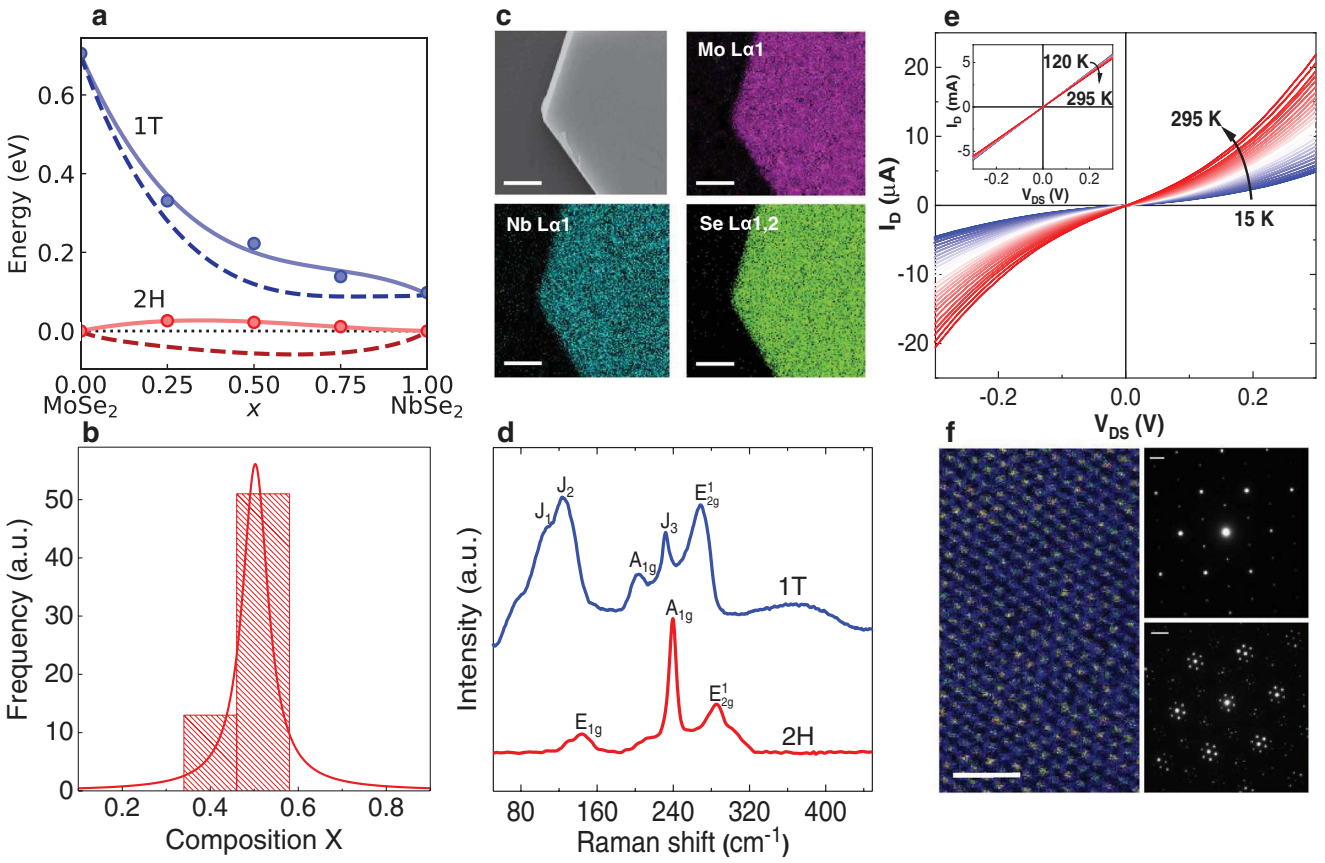

Figure 1. Summary of characterization of $Mo_{1-x}Nb_xSe_2$ alloy. a) Enthalpy (solid lines) and free energy at T = 1350 K (dashed lines) of *1T* and *2H* $Mo_{1-x}Nb_xSe_2$ based on cubic fits to calculated enthalpy values (circles). b) EDX frequency distribution of $Mo_{1-x}Nb_xSe_2$ sample obtained from measurements on ≈50–60 flakes. c) EDX–SEM elemental maps obtained from the $Mo_{1-x}Nb_xSe_2$ flake (scale bar: 1 μm). d) Raman spectra of few-layer $Mo_{1-x}Nb_xSe_2$ with *1T* and *2H* phases. Raman spectra are shifted vertically for clarity. e) Temperature-dependent current-voltage (I_D–V_{DS}) transport characteristics of *1T* $Mo_{1-x}Nb_xSe_2$ and *2H* $Mo_{1-x}Nb_xSe_2$ (top inset). f) The atomic-resolution HAADF of $Mo_{1-x}Nb_xSe_2$ (left, scale bar: 1 nm), and diffraction patterns from *2H* (top, scale bar: 2 nm^{-1}) and *1T* $Mo_{1-x}Nb_xSe_2$ flakes (bottom, scale bar: 2 nm^{-1}), respectively, (right).

2. Results and discussion

We selected an equimolar alloy of $MoSe_2$, a semiconductor, and $NbSe_2$, a metal. To determine the synthesis temperatures required to achieve a disordered $Mo_{1-x}Nb_xSe_2$ alloy, first-principles density-functional theory (DFT) was used to calculate an equilibrium phase diagram. This phase diagram predicts the miscibility temperature, T_{misc}, above which the alloy prefers the disordered, homogeneous phase over phase separation. The phase diagram is generated by looping over a grid of temperature values and determining the binodal and spinodal boundaries with the common tangent construction and curvature of the free energy, respectively (Section S1, Supporting Information).[14] **Figure 1**a shows the enthalpy and the free energy at the synthesis temperature (1350 K) of the *1T* and *2H* phases of $Mo_{1-x}Nb_xSe_2$. The *2H* phase is predicted to be more stable at every molar concentration over the *1T* phase, but it is immiscible at T = 0 K due to a positive mixing enthalpy. However due to increasing configurational entropy with temperature, at 1350 K, we find the free energy of the *2H* phase to be negative with a positive curvature everywhere, which inhibits phase segregation. Figure S1, Supporting Information, shows the detailed phase diagram of the *2H* phase where the miscibility temperature is seen to be 900 K.

In addition, the change in stability of the *1T* phase of $Mo_{1-x}Nb_xSe_2$ upon alloying is shown in Figure 1a. While the *1T* phase remains metastable for the entire compositional range, it has a negative mixing enthalpy when compared to the energy of the *1T* phase of $MoSe_2$ and $NbSe_2$, making a 1T solid solution favorable to 1T phase segregation. At x = 0.5 and a temperature of T = 1350 K, the free energy difference between *1T* and *2H* phases is 176 meV per formula unit.

We synthesized the bulk crystals of $Mo_{1-x}Nb_xSe_2$ at 1350 K using a chemical vapor transport (CVT) method with an equimolar chemical composition of x = 0.5. Growth was carried out by maintaining the temperature gradient between the source (hot) and the growth (cold) zone of the reaction ampule. Subsequently, the crystallization occurs at both source and growth zones, where a high-quality *1T* and *2H* phases were obtained (Figure S2, Supporting Information). $Mo_{1-x}Nb_xSe_2$ nanoflakes of *2H* and *1T* phases were mechanically exfoliated and characterized by energy-dispersive X-ray spectroscopy (EDX) in scanning electron microscopy (SEM), Raman spectroscopy and electrical measurements. SEM-EDX was employed to find the distribution of elemental composition in ≈50–60 flakes, verifying the well-defined composition of $x \approx 0.5$ (Figure 1b and Figure S3, Supporting Information). Moreover, Figure 1c shows the uniform distribution of Mo and Nb cations through a homogenous EDX composition map for the synthesized flakes.

Raman spectra of the two different phases of $Mo_{1-x}Nb_xSe_2$ were collected from the exfoliated few-layer flakes, which show distinct vibrational features (Figure 1d). For the *2H* phase, the three characteristic Raman peaks of in-plane (E_{1g}), out-of-plane (A_{1g}) and $E_{2g}{}^1$ vibrational modes are at 143.5 cm^{-1}, 239.7 cm^{-1} and 285.5 cm^{-1}, respectively. These peaks are positioned between those of the two end members, *2H*-$MoSe_2$[15,16] and *2H*-$NbSe_2$[17,18] (Figure S4, Supporting Information). In the *1T* phase, $E_{2g}{}^1$ and A_{1g} have shifted to 268.4 cm^{-1} and 231.7 cm^{-1} and three of the signature peaks of octahedral structure corresponding to superlattice formation, J_3, J_2, and J_1, appeared at 203.2 cm^{-1}, 123.8 cm^{-1} and 106 cm^{-1}, respectively.[19,20] To characterize the electronic behavior of *1T* and *2H* phases, field-effect transistors (FETs) were fabricated on the same flakes using a SiO_2/Si (≈300 nm/0.5 mm) substrate. The current-voltage transport characteristics (I_{ds}–V_{ds}) of representative devices tested in the 15–295 K temperature range are shown in Figure 1e. Figure 1e and the top inset show the I_D–V_{DS} curves versus temperature for the four-probe tested *1T* and *2H* phase $Mo_{1-x}Nb_xSe_2$ devices, respectively. The bias was swept from –0.3 V to 0.3 V and the devices showed two different electrical behaviors, which was illustrated by the decreasing and increasing trend of the current versus temperature. These results indicate metallic and semiconducting behaviors for the *2H* and *1T* alloys at room temperature, respectively.[21–25]

We also performed X-ray photoelectron spectroscopy (XPS) on the synthesized alloy to characterize their chemical states (Figure S5, Supporting Information). Figure S5a, Supporting Information, shows the two main peaks of the Mo spectrum located at 227.9 and 230.9 eV corresponding to Mo $3d_{5/2}$ and Mo $3d_{3/2}$.[26] The Nb 3d region in Figure S5b, Supporting Information, shows two major peaks at 203.04 eV and 205.8 eV assigned to Nb $3d_{5/2}$ and Nb $3d_{3/2}$, respectively.[27] Figure S5c, Supporting Information, represents the Se 3d spectrum of $Mo_{1-x}Nb_xSe_2$ located at 53.4 and 54.3 eV corresponding to $3d_{5/2}$ and $3d_{3/2}$,[26,27] respectively. X-ray absorption near-edge spectroscopy (XANES) measurements of $MoSe_2$, $NbSe_2$ and $Mo_{1-x}Nb_xSe_2$ (Section S6, Supporting Information) revealed that the average electronic state of the different elements in the alloy samples was similar to the respective end members. Additionally, to characterize the crystal structure of the synthesized alloys, XRD measurements were performed which confirms the successful synthesis of the material by comparing to the endmembers $MoSe_2$ and $NbSe_2$ (Figure S7, Supporting Information).

Figure 1f shows a typical atomic-resolution high-angle annular dark-field (HAADF) of an isolated crystal containing the *1T* alloy, viewed along the [001] projection. In this imaging mode, the intensity of the atomic column is proportional to Z^2, the atomic number squared.[28] Hence, only the heavier Mo/Nb atomic columns are visible in the HAADF image, which form a triangular lattice. Furthermore, due to their similar atomic numbers, Mo (Z = 42) and Nb (Z = 41) atomic columns have similar intensities and are indistinguishable. The insets in Figure 1f show two different diffraction patterns. The *2H* and *1T* phases are represented in the top and bottom panels, respectively. While the *2H* diffraction pattern only shows peaks from the underlying layered lattice, the *1T* diffraction has additional peaks suggesting the existence of a superlattice. The source of these additional peaks will be discussed below. The locations and intensities of the Bragg peaks allow us to exclude the *R3m, 1T′,* and *1Td* phases (Figures S8 and S9, Supporting Information).

To gain more insight into the electronic structure of the semiconducting *1T*-$Mo_{1-x}Nb_xSe_2$ flakes, scanning tunneling microscopy/spectroscopy (STM/STS) was performed on mechanically exfoliated few-layer flakes using a SiC/graphene substrate. **Figure 2**a shows a high-resolution STM image obtained in ultrahigh vacuum (<10^{-10} Torr) at liquid nitrogen temperatures (77 K). The RMS roughness of the surface in Figure 2a (50×50 nm^2) is ≈0.5 Å and the contrast of the STM image was adjusted to resolve and highlight internal dopants near the first layer, whose local density states (LDOS) are available to tunneling with STM. To clearly observe the hexagonal pattern, a magnified view of the selected region is shown in Figure 2b. A fast Fourier transform (FFT) of the image indicates the hexagonal structure of the lattice plane (inset Figure 2a). An average periodicity of ≈0.3 nm from peak-to-peak was observed from the line profile (marked with the blue and red line in Figure 2b), which is in good agreement with the lattice constant calculated from the FFT pattern (Section S9, Supporting Information). Figure 2d displays *I*–*V* (red) and dI/dV–*V* (blue) curves acquired at 77 K. Notably, an electronic bandgap of 0.55 eV was observed from the spectra. Moreover, multiple measurements indicate that the range of bandgap varies between 0.42–0.58 eV (Figure S11, Supporting Information). The positions of the band edges relative to the Fermi level reveals a p-type behavior.

To connect the electronic behavior of *1T*-$Mo_{1-x}Nb_xSe_2$ to its structure, we revisit its electron diffraction pattern. The results of the TEM diffraction experiments for *1T*-$Mo_{1-x}Nb_xSe_2$ flakes are shown enlarged and false-colored in **Figure 3**a. At the center is the gamma peak marked in blue. The primary and secondary Bragg peaks, which are corresponding to unit cell periodicity, are indexed in green and red, respectively. Using the location of the fundamental Bragg peaks, the lattice parameter is determined to be (3.29 ± 0.01) Å. A triangular sub-lattice of the Mo and Nb columns would only show the gamma and fundamental Bragg peaks, but additional peaks were observed here. We refer to the superlattice peaks surrounding even-ordered peaks of the triangular sub-lattice (pink in Figure 3a) as "petals" because of their resemblance to flower petals. These petals have a six-fold symmetry around their associated fundamental Bragg peak. The radial distance of the petals to their associated fundamental Bragg peak is approximately a quarter of the distance between the fundamental Bragg peaks and the gamma peak. This factor of ≈1/4 in the reciprocal space indicates the existence of an additional periodicity corresponding to a $\approx 4 \times 4$ supercell of the *1T*-phase unit cell. However, a closer inspection of the gamma peak and one of the primary Bragg peaks (Figure 3b) shows that a perfect 4×4 supercell cannot cause these petal peaks. The imposed arrows in Figure 3b represent wave vectors of one of the petals and the primary Bragg peak, and they are evidently not parallel. In fact, they are rotated by ≈4.14° (Section S11, Supporting Information).

A magnified view of the primary Bragg peak (010) with surrounding superstructure reflections is shown in Figure 3c. The pattern was labeled using a 5-index convention with the first 3 indices corresponding to the associated Bragg peak and the last 2 indices denoting the location of the superstructure peak. An

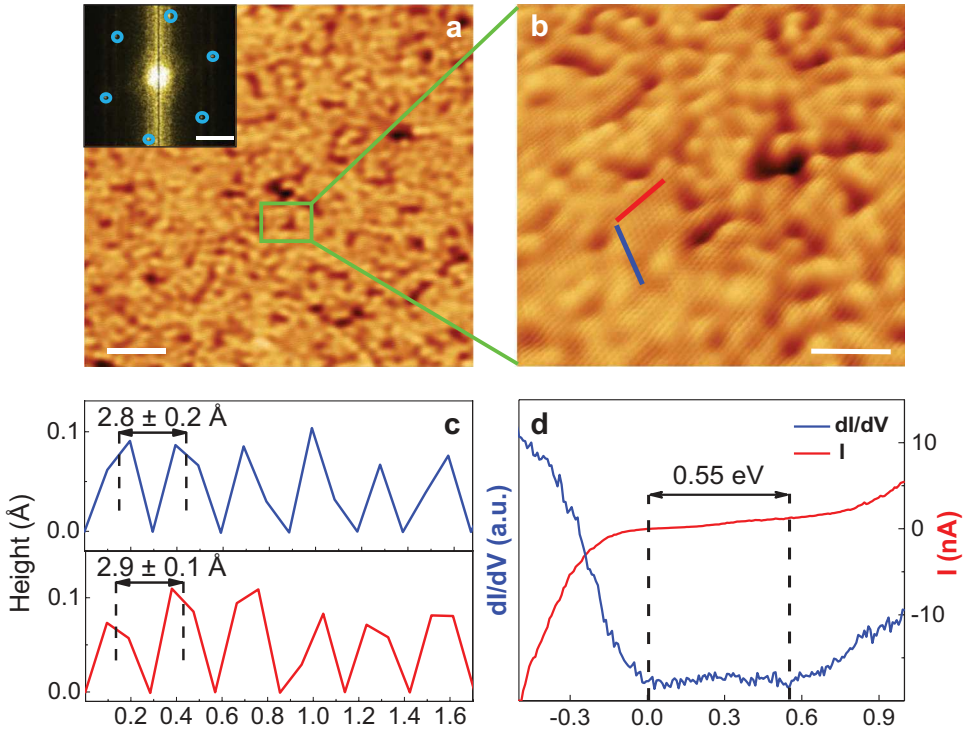

Figure 2. Summary of STM/STS results. a) High resolution STM image of *1T* $Mo_{1-x}Nb_xSe_2$ flake on a SiC/graphene substrate (STM imaging conditions: Sample Bias: 200 mV, and Setpoint Current: 2 nA, scale bar: 10 nm). Inset shows FFT pattern of flake in panel a), which indicates hexagonal lattice structures (scale bar: 2 nm^{-1}). b) A zoom-in view of the area marked by the white square in panel a) shows a clear hexagonal lattice structure (scale bar: 2 nm). c) Height profiles following the direction of blue and red lines in panel (b). d) STS results of *dI*/*dV* (blue) and *I*–*V* (red) curves reveals a p-type behavior with a 0.55 eV electronic bandgap.

important observation to note here is that the superstructure peaks with all integer indices correspond exactly to the petals surrounding the even-ordered Bragg peaks. Two corollaries to this observation are that the superstructure peaks are also rotated by the same angle with respect to the fundamental Bragg peaks and that the superstructure peaks are $\frac{1}{\sqrt{3}}$ times the distance from each other as the petals are. As discussed in Section S11, Supporting Information, we can rule out the twisting between layers to form Moiré patterns as the origin of the superlattice peaks.

In addition to diffraction information, STEM-annular bright-field (ABF), which is sensitive to lattice distortions,[29] was also used to analyze the *1T* alloy. Figure 3d shows a STEM-ABF image with bright spots arranged in a triangular pattern with an overall pattern of periodic white splotches arranged in a 4×4 pattern (for a higher resolution image, see Figure S16, Supporting Information). Because these changes in image contrast in STEM-ABF correspond to local strain,[30] these results provide additional support for an $\approx 4 \times 4$ supercell caused due to periodic lattice distortions.

The bright petal peaks in the diffraction pattern and periodic splotches in the STEM-ABF image together with the additional weak superstructure peaks indicate the existence of periodic lattice distortions due to charge density waves (CDWs) in the disordered $Mo_{1-x}Nb_xSe_2$ alloy with *1T* phase. CDWs are periodic waves of electron density in a crystal. The presence of periodic, high concentrations of electrons attract ions and causes periodic distortions in the lattice that can be detected through diffraction. The rotated petals in the diffraction pattern can be explained by what are known as nearly commensurate CDWs (NCCDWs).[31] A NCCDW phase is characterized by CDWs that are nearly commensurate with the underlying lattice. In this case, the periodicity of the NCCDW appears to be a 4×4 supercell that is rotated $\approx 4°$ from the ionic lattice, thus explaining the rotated petals in the diffraction pattern. The locations of the petal peaks correspond to low-order superpositions of CDW wave vectors while the superstructure peaks are located at high-order superpositions of CDW wave vectors (Figure S13, Supporting Information). The lack of drift of the splotches at $\approx 4°$ with respect to the lattice observed in the STEM-ABF image in Figure 3d is explained by a key feature of NCCDWs. Because they are nearly commensurate, they tend to be commensurate over large domains; and when they start to become out of phase with the lattice, they phase-slip back in phase with the lattice. In the case of *1T*-$Mo_{1-x}Nb_xSe_2$, the NCCDWs locally cause 4×4 distortion patterns in phase with the lattice. As the CDW begins to become out-of-phase with the lattice, phase slips realign the CDW with the lattice. See Figure S15, Supporting Information, for a diagram of the domain structure of the NCCDW phase. This phenomenon of phase slipping between commensurate domains may contribute to the overall inhomogeneity of intensity in Figure 3d (Section S12, Supporting Information).

CDWs can also result in the opening of a bandgap[32–34] such as that observed in the *1T* phase of $Mo_{1-x}Nb_xSe_2$. We used DFT calculations to further examine the electronic structure of the

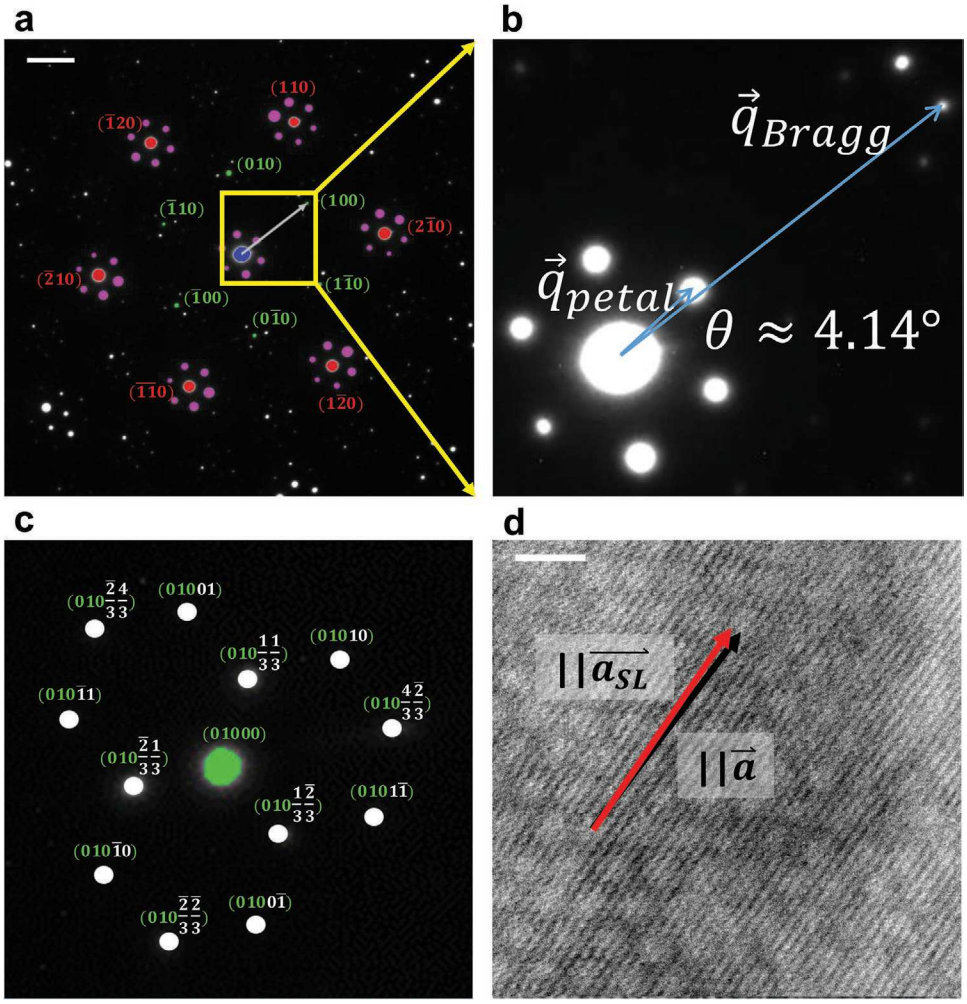

Figure 3. a) Electron beam diffraction pattern of *1T* $Mo_{1-x}Nb_xSe_2$ showing superlattice features (indexed using 5-digit notation). The fundamental and secondary reflections are shown in green and red, respectively, with "petal" reflections surrounding the secondary reflections shown in pink, (scale bar: 2 nm^{-1}). b) The gamma peak, its petals, and the primary peak (100). Arrows indicate wave vectors of the lattice (Bragg) and the superlattice distortion (petal). c) Magnified view of the (010) diffraction spots showing non-integer superlattice reflections. d) The Atomic-resolution bright field image of *1T* $Mo_{1-x}Nb_xSe_2$ (001) (scale bar: 2 nm). The red and black arrows show the direction of the superlattice distortion and atomic lattice, respectively.

two phases of $Mo_{1-x}Nb_xSe_2$ and elucidate how an alloy of *2H*-$MoSe_2$, a semiconductor, and *2H*-$NbSe_2$, a metal, produces a semiconductor in the *1T* phase (*1T*-$MoSe_2$ and *1T*-$NbSe_2$ are metals at room temperature). As in our experimental synthesis, we use the equimolar condition of $x = 0.5$. We observe the presence of large local distortions in the DFT-optimized special quasirandom structure[35] representing *1T*-$Mo_{0.5}Nb_{0.5}Se_2$, as shown in **Figure 4**a. Figure 4b shows the histogram of TM-Se bond lengths in *1T*-$Mo_{0.5}Nb_{0.5}Se_2$ along with their values for pure *1T*-$MoSe_2$ and *1T*-$NbSe_2$ for reference. The distortions are quantitatively evident from the large spread in bond lengths that extend beyond the pure TMDC references. In contrast, the *2H*-$Mo_{1-x}Nb_xSe_2$ showed relatively smaller distortions (Figures S17–S20, Supporting Information). The effects of distortion on the electronic properties of *1T*- and *2H*-$Mo_{1-x}Nb_xSe_2$ are shown in Figure 4c in the form of projected density of states (DOS) of the TM atoms. The top two panels show DOS of the pure TMDCs; *1T*-$MoSe_2$, *1T*-$NbSe_2$, and *2H*-$NbSe_2$ are metallic while *2H*-$MoSe_2$ has a bandgap, as reported in the literature.[36–38] The middle two panels show the TM-projected DOS for optimized $Mo_{1-x}Nb_xSe_2$ with local distortions. We observe the opening up of a small band gap in the *1T* phase, while the *2H* phase maintains metallic character. To ensure that the opening of the band gap was general to supercell size, 4×4, 6×6, and 8×8 supercells were tested (Section S14, Supporting Information). To determine how distortions play a role in the opening of the bandgap, the bottom panels show the TM-projected DOS of the alloys without allowing the ions to relax. It is seen that clamping the ions causes *1T*-$Mo_{1-x}Nb_xSe_2$ to lose its bandgap, confirming the importance of lattice distortions to bandgap opening. While the large size of the supercell created due to the NCCDW observed from electron diffraction measurements and illustrated in an atomic model in Figure S15, Supporting Information) prohibits calculation of its total energy, it is reasonable to expect that the periodic lattice distortions created by the NCCDW will be energetically more favorable than the random local distortions captured in the smaller atomic model.

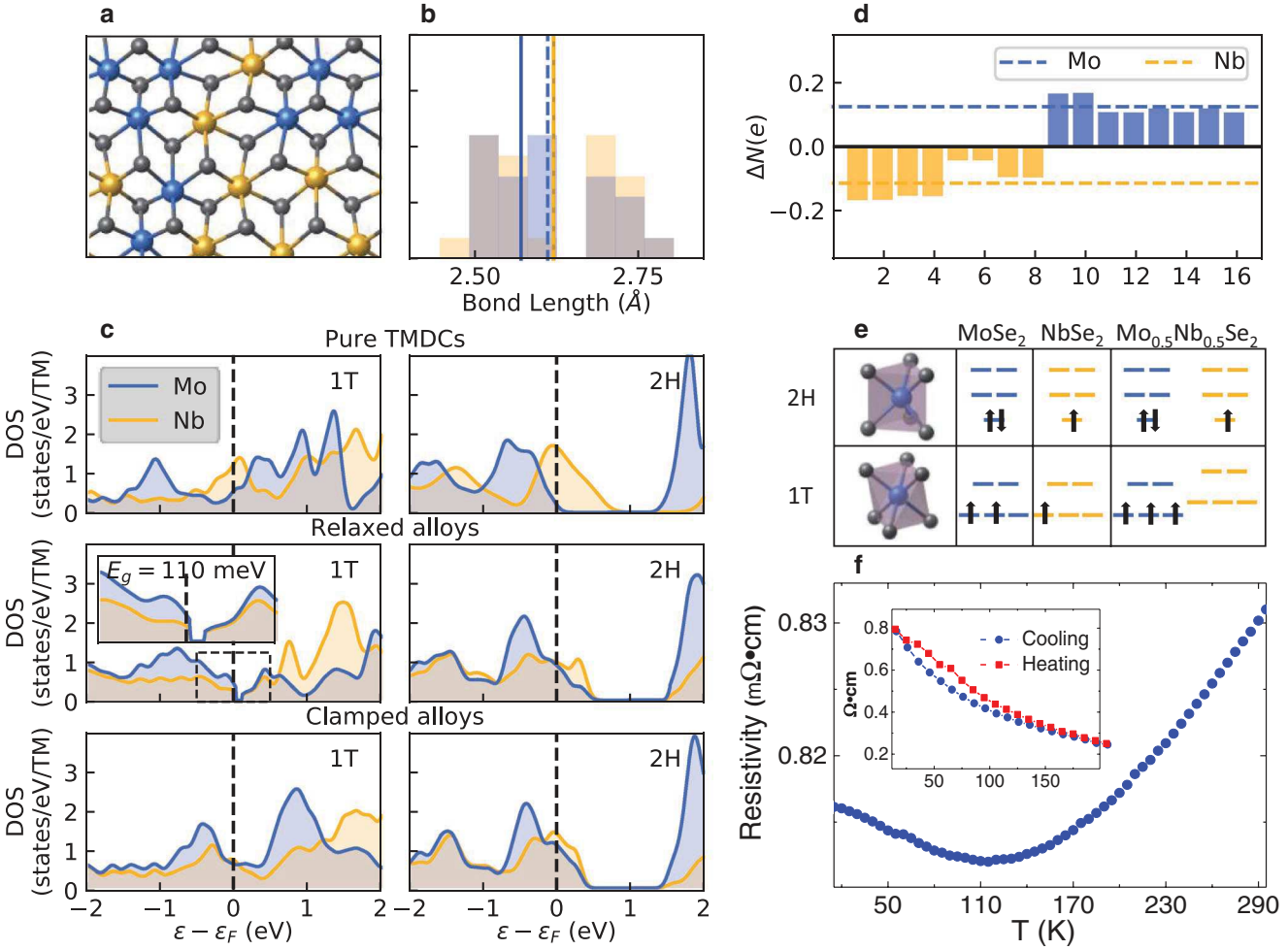

Figure 4. Density function theory (DFT) simulation. a) Schematic diagram of the crystal structure of *1T*-$Mo_{1-x}Nb_xSe_2$ with prominent distortions, shown with Nb in yellow, Mo in blue and Se in grey. b) A histogram of TM-Se bond lengths of *1T*-$Mo_{1-x}Nb_xSe_2$. Solid and dashed vertical lines correspond to the pure TMDC bond lengths and average alloy bond lengths, respectively. c) The transition metal-projected DOS for the *1T* and *2H* phases (left and right columns) of the pure TMDC phase (top row), the relaxed alloys (middle row), and the alloys with TM ions fixed (bottom row). d) The relative electron transfers in *1T*-$Mo_{1-x}Nb_xSe_2$ going from clamped to relaxed for all 16 TMs in the 4 × 4 supercell with averages marked with dashed lines. e) Schematic crystal field splitting diagrams for $MoSe_2$, $NbSe_2$, and *1T*-$Mo_{1-x}Nb_xSe_2$ (left, center, and right, respectively) for the *2H* and *1T* phases (top and bottom). f) Temperature-dependent resistivity of *2H*-$Mo_{1-x}Nb_xSe_2$. Inset shows temperature-dependent resistivity of *1T*-$Mo_{1-x}Nb_xSe_2$ with the cooling and heating process.

To further examine how local distortions can cause the opening-up of a bandgap in *1T*-$Mo_{1-x}Nb_xSe_2$ but not in the *2H* phase, Bader charge analysis was performed on the relaxed and clamped alloys.[39–43] This technique allows the partitioning of electrons in a solid to ions by summing over a volume around each ion defined by zero flux surfaces of the electron density. By comparing the number of electrons on each cation before and after relaxation, the charge transfer due to distortions can be determined. The difference in electron occupation between the relaxed (with distortions) and clamped structures for each TM in the 4 × 4 supercell is shown in Figure 4d. These results show a transfer of electrons from Nb to Mo upon relaxation, indicating that the lattice distortions are associated with charge transfers (for an analysis of the *2H*-phase, see Section S15 in Supporting Information). Figure 4e shows the crystal-field splitting of pure $MoSe_2$, $NbSe_2$, and the $Mo_{1-x}Nb_xSe_2$ alloy in both *1T* and *2H* phases. The trigonal prismatic coordination of the Se atoms around the Mo and Nb atoms in the *2H* phase splits the five 4d-states into three groups with the d_{z^2} states at the lowest energy, followed by doubly degenerate d_{xy} and $d_{x^2-y^2}$ states at intermediate energy, and another pair of degenerate d_{yz} and d_{xz} states at highest energy. The octahedral coordination of the *1T* phase, instead, splits the five d-states into triply degenerate d_{xy}, d_{yz} and d_{xz} states at a lower energy and doubly degenerate d_{z^2} and $d_{x^2-y^2}$ states at a higher energy. Electron filling into these crystal-field split states provides a simple explanation for the metallic behavior of *2H* and *1T*-$NbSe_2$, and *1T*-$MoSe_2$, and the semiconducting behavior of *2H*-$MoSe_2$. Furthermore, the higher electronegativity of Mo pulls its 4d states to lower energy than that of Nb. Consequently, in *1T*-$Mo_{1-x}Nb_xSe_2$, an electron transfers from Nb to Mo results in the half-filling of the triply degenerate states of Mo atoms and an emptying of the Nb states, which opens up a band gap as observed in Figure 4c. However, in *2H*-$Mo_{1-x}Nb_xSe_2$, the lower energy d_{z^2} states are $3/4^{th}$ full, which makes them metallic as observed experimentally. We note that this crystal field splitting analysis eliminates

the need to invoke Mott insulation, which is observed in systems with strong electron-electron interactions, such as in monolayer *1T*-$NbSe_2$.[32,38]

To investigate the possibilities of CDW phase transitions in both *1T* and *2H* phases, electrical transport measurements were taken over a range of temperatures. The electrical resistivity of devices fabricated on both *1T* and *2H* phase alloys were measured using the four-probe configuration. For the *1T*-$Mo_{1-x}Nb_xSe_2$, a well-defined semiconducting behavior was observed in the 15–295 K temperature range, for both cooling and heating processes (inset in Figure 4f). A hysteresis between warming and cooling cycles indicates a first-order phase transition between NCCDW and CCDW phases. For the *2H*-$Mo_{1-x}Nb_xSe_2$, at higher temperatures, the resistivity, ρ(T), decreases with decreasing temperatures which is fully consistent with the expected metallic behavior. A clear upturn in resistivity was observed on decreasing temperature at ≈120 K (Figure 4f). The emergence of this anomaly in the temperature-dependent resistivity measurements indicates the abrupt opening of a bandgap, indicating a transition to a CDW phase.[44,45] We also found that the transition temperature is strongly thickness-dependent, which is consistent with CDW transitions in other 2D materials.[46,47]

3. Conclusion

In summary, we have demonstrated a phase-dependent bandgap engineering in $Mo_{1-x}Nb_xSe_2$ as an example of semiconductor-metal alloying. In contrast to the expected, the metallic behavior of the alloy, bandgaps with the range of 0.42–0.58 eV were demonstrated in the *1T* structure. Our crystal structure analysis and DFT calculations showed the *1T* phase to be susceptible to distortions that open a band gap. This susceptibility to distortions likely facilitates the multiple observed CDW phases, including a NCCDW phase confirmed by electron diffraction measurements and a low temperature CCDW confirmed by a hysteresis loop in the resistivity. Moreover, a metal-insulator transition associated with a CDW phase transition was observed at ≈120 K in the *2H*-$Mo_{1-x}Nb_xSe_2$. This work provides a new way to tailor an electronic band structure of non-isovalent alloys for applications in various (opto)-electronics and (photo)-electrochemical systems.

4. Experimental Section

Computational Details: Monolayer alloys were simulated using special quasi-random structures (SQSs)[35] generated using the alloy theoretic automated toolkit (ATAT).[48] A vacuum spacing of >15 Å was used to reduce the interaction between image planes due to the use of periodic boundary conditions. Total energies, charge densities, and densities of states were calculated using density-functional theory (DFT) as implemented in VASP using the Perdew-Burke-Ernzerhof exchange-correlation functional.[49,50] *k*-points meshes were generated using the Monkhorst-Pack method.[51] *k*-points grids of $n_x \times n_y \times 1$, where $n_i \approx 25$ Å/a_i for relaxations and $n_i \approx 75$ Å/a_i for static calculations with a_i being the lattice parameter in the *i*th direction. A kinetic energy cutoff of 450 eV was used for all the calculations.

Material Synthesis: Bulk $Mo_{1-x}Nb_xSe_2$ (x = 0.5) crystals were synthesized through chemical vapor transport (CVT) method. The elemental powder molybdenum (99.99% Sigma Aldrich), niobium (99.5% Sigma Aldrich), and selenide (99.99% Sigma Aldrich) were measured based on stoichiometric ratio and mixed. Before evacuation with a high vacuum (10^{-5} torr), the quartz ampoules with 15 cm inner transport length were thoroughly cleaned with 10% diluted Hydrofluoric acid (HF) followed by cleaning with DI water and annealing at 1050 °C to remove the possible residues and create nucleation sitting spots. The growth process started with 50 °C h^{-1} to reach 1080 °C and then maintained the 150 °C temperature gradient between source and growth zones. After 5-day growth and followed by slowly cooling to room temperature, we got crystalline materials from both zones.

SEM: High-resolution SEM images were obtained on FEI Quanta 650 ESEM system integrated with the Oxford AZtec EDS and EBSD to perform the EDX analysis.

Raman spectroscopy: Raman Spectroscopy was performed at room temperature and ambient conditions using the HORIBA LabRAM HR Evolution confocal Raman microscope, equipped with a Horiba Andor detector. A 532 nm laser was employed for excitation with the spot diameter of ≈1.3 µm, to limit the laser intensities to less than 8 µW $µm^{-2}$.

Electron Microscopy Analysis: The STEM characterization was performed on the exfoliated samples using the aberration-corrected UIC JEOL ARM200CF STEM equipped with a cold field emission gun operated at 200 kV and a Gatan Continuum EEL spectrometer, providing a sub–Å probe-size and 350 meV energy resolution. An electron probe convergence semi-angle of 24 mrad was used and annular bright-field (ABF) images were acquired using an inner detector angle of 12 mrad and an outer angle of 24 mrad. The electron diffraction data were acquired using the JEOL3010 at UIC, which is conventional high-resolution TEM equipped with a LaB6 electron source operating at 300 kV.

XRD: XRD patterns of exfoliated $Mo_{1-x}Nb_xSe_2$, $MoSe_2$, and $NbSe_2$ were performed on a Bruker D8 Avance using a Cu Kα (λ_{avg} = 1.5418 Å) radiation.

XPS: XPS was performed on the powder samples, using a Thermo Scientific ESCALAB 250Xi instrument. Analysis and peak fitting were carried out using the Thermo Avantage software.

AFM: Atomic force microscopy (AFM) images were obtained using tapping mode of Bruker Dimension Icon AFM with ScanAsyst in air.

Device Fabrication: Few-layer $Mo_{1-x}Nb_xSe_2$ flakes were mechanically exfoliated on 300 nm SiO_2/Si substrates. Electron Beam Lithography (EBL) was employed to write the four probe pattern on the PMMA coated samples to fabricate the transistor devices. The Cr/Au (5/50 nm) electrodes were deposited by the Angstrom EvoVac electron beam evaporator.

Electrical Measurement: Devices were tested with sweeping bias voltages from −0.3 to 0.3 V in terms of different temperatures to determine the electrical properties. In addition, the temperature–dependent resistance measurements were produced by MATLAB codes with a Keithley 2612A source meter to illustrate the CDW phase transitions. A homemade cryostat was employed to control the varying temperatures and all the measurements were operated in a high vacuum cryogenic chamber (10^{-8} to 10^{-7} torr).

STM and STS: STM and STS measurements were performed at both room temperature and liquid nitrogen temperature (77K) under ultrahigh vacuum (1×10^{-11} torr) using a commercial Omicron variable temperature microscope. STM images were obtained with a sample bias of 200 mV and a setpoint current of 2 nA. STS measurements where made using a lock-in amplifier with a dither amplitude of 30 mV and frequency of 10 kHz.

XANES: All the X-ray absorption measurements were done at the Materials Research Collaborative Access Team (MRCAT) Sector 10-BM beamline at the Advanced Photon Source (APS) located at Argonne National Laboratory. Measurements were done in transmission mode for Se K edge (Eo = 12.6 keV) and Mo K edge (Eo = 20 keV) using ionization gas chambers filled with 10% N and 90% Ar, and >99% Ar, <1% N respectively. The Se foil and Mo foil were placed between the second and third gas chamber. Powder samples were diluted 25 wt% with cellulose and pressed to form pellets and sealed in Kapton tape. The XANES data were reduced using the ATHENA program and fitted to structural models using the ARTEMIS program.

Supporting Information

Supporting Information is available from the Wiley Online Library or from the author.

Acknowledgements

The work of A.S.-K., R.F.K., S.W., Z.H., L.M., R.D. and A.R. was supported by the National Science Foundation DMREF Grant 1729420. J.C. and R.M. acknowledge support through NSF DMREF-1729787. H.G. and F.K.-A. acknowledge the support by NSF-EFRI-1740876. K.K. and J.C. acknowledge the support by the National Science Foundation through award CBET-1800357. Use of the Center for Nanoscale Materials, an Office of Science user facility, was supported by the U.S. Department of Energy, Office of Science, Office of Basic Energy Sciences, under Contract No. DE-AC02-06CH11357. The authors acknowledge the use of the Nanotechnology Core Facility and the Research Resources Center at the University of Illinois at Chicago. The acquisition of UIC JEOL JEM ARM200CF was supported by an MRI-R^2 grant from the National Science Foundation (Grant No. DMR-0959470) and the upgraded Gatan Continuum spectrometer was supported by a grant from the NSF (DMR-1626065). This work made use of the Pritzker Nanofabrication Facility at the University of Chicago, as well as the EPIC facility of Northwestern University's NUANCE Center and Raman facility at the University of Chicago's MPML supported by the MRSEC program of the National Science Foundation (DMR-1720139), and the Soft and Hybrid Nanotechnology Experimental (SHyNE) Resource (NSF ECCS-1542205). This work made use of instruments in the Electron Microscopy Core of UIC's Research Resources Center. Use of the Advanced Photon Source at Argonne National Laboratory was supported by the U.S. Department of Energy, Office of Science, Office of Basic Energy Sciences, under Contract No. DE-AC02-06CH11357.

Conflict of Interest

The authors declare no conflict of interest.

Author Contributions

S.W., J.C., Z.H. contributed equally to this work. A.S.-K. and F. K.-A. led the material synthesis and electronic experiments. R.M. led the computational studies. S.W. and Z.H. synthesized the materials. J.C. and R.M. performed the theoretical calculations and assisted with the analysis and interpretation of the microscopy results. N.G. carried out STM/STS measurements. Z.H. performed EDX and SEM characterizations. S.W. carried out Raman, AFM and device nanofabrication. S.W., Z.H., and H.G. performed electrical measurements. A.R., R.D. and R.F.K. performed the (S)TEM characterization. K.K. and J.C. performed XRD and XANES experiments and analysis. L.M. carried out XPS.

Keywords

alloy, bandgap engineering, charge density wave, density functional theory, transition metal dichalcogenides

Received: June 9, 2020
Revised: August 27, 2020
Published online:

[1] K. F. Mak, C. Lee, J. Hone, J. Shan, T. F. Heinz, *Phys. Rev. Lett.* **2010**, *105*, 136805.
[2] K. Kang, K. H. Lee, Y. Han, H. Gao, S. Xie, D. A. Muller, J. Park, *Nature* **2017**, *550*, 229.
[3] M. Mahjouri-Samani, M. W. Lin, K. Wang, A. R. Lupini, J. Lee, L. Basile, A. Boulesbaa, C. M. Rouleau, A. A. Puretzky, I. N. Ivanov, K. Xiao, M. Yoon, D. B. Geohegan, *Nat. Commun.* **2015**, *6*, 7749.
[4] Y. Gong, J. Lin, X. Wang, G. Shi, S. Lei, Z. Lin, X. Zou, G. Ye, R. Vajtai, B. I. Yakobson, H. Terrones, M. Terrones, B. K. Tay, J. Lou, S. T. Pantelides, Z. Liu, W. Zhou, P. M. Ajayan, *Nat. Mater.* **2014**, *13*, 1135.
[5] P. Johari, V. B. Shenoy, *ACS Nano* **2012**, *6*, 5449.
[6] C. Ning, L. Dou, P. Yang, *Nat. Rev. Mater.* **2017**, *2*, 17070.
[7] S. Susarla, A. Kutana, J. A. Hachtel, V. Kochat, A. Apte, R. Vajtai, J. C. Idrobo, B. I. Yakobson, C. S. Tiwary, P. M. Ajayan, *Adv. Mater.* **2017**, *29*, 1.
[8] Y. Chen, J. Xi, D. O. Dumcenco, Z. Liu, K. Suenaga, D. Wang, Z. Shuai, Y. S. Huang, L. Xie, *ACS Nano* **2013**, *7*, 4610.
[9] M. Zhang, J. Wu, Y. Zhu, D. O. Dumcenco, J. Hong, N. Mao, S. Deng, Y. Chen, Y. Yang, C. Jin, S. H. Chaki, Y.-S. Huang, J. Zhang, L. Xie, *ACS Nano* **2014**, *8*, 7130.
[10] J. Zhou, J. Lin, X. Huang, Y. Zhou, Y. Chen, J. Xia, H. Wang, Y. Xie, H. Yu, J. Lei, D. Wu, F. Liu, Q. Fu, Q. Zeng, C.-H. Hsu, C. Yang, L. Lu, T. Yu, Z. Shen, H. Lin, B. I. Yakobson, Q. Liu, K. Suenaga, G. Liu, Z. Liu, *Nature* **2018**, *556*, 355.
[11] J. Park, M. S. Kim, B. Park, S. H. Oh, S. Roy, J. Kim, W. Choi, *ACS Nano* **2018**, *12*, 6301.
[12] A. Kutana, E. S. Penev, B. I. Yakobson, *Nanoscale* **2014**, *6*, 5820.
[13] H. Luo, W. Xie, J. Tao, I. Pletikosic, T. Valla, G. S. Sahasrabudhe, G. Osterhoudt, E. Sutton, K. S. Burch, E. M. Seibel, J. W. Krizan, Y. Zhu, R. J. Cava, *Chem. Mater.* **2016**, *28*, 1927.
[14] Z. Hemmat, J. Cavin, A. Ahmadiparidari, A. Ruckel, S. Rastegar, S. N. Misal, L. Majidi, K. Kumar, S. Wang, J. Guo, R. Dawood, F. Lagunas, P. Parajuli, A. T. Ngo, L. A. Curtiss, S. B. Cho, J. Cabana, R. F. Klie, R. Mishra, A. Salehi-Khojin, *Adv. Mater.* **2020**, *32*, 1907041.
[15] D. Nam, J. U. Lee, H. Cheong, *Sci. Rep.* **2015**, *5*, 17113.
[16] P. Tonndorf, R. Schmidt, P. Böttger, X. Zhang, J. Börner, A. Liebig, M. Albrecht, C. Kloc, O. Gordan, D. R. T. Zahn, S. Michaelis de Vasconcellos, R. Bratschitsch, *Opt. Express* **2013**, *21*, 4908.
[17] X. Zhang, Q. H. Tan, J. B. Wu, W. Shi, P. H. Tan, *Nanoscale* **2016**, *8*, 6435.
[18] C. M. Pereira, W. Y. Liang, *J. Phys. C Solid State Phys.* **1982**, *15*, L991.
[19] S. Jiménez Sandoval, D. Yang, R. F. Frindt, J. C. Irwin, *Phys. Rev. B* **1991**, *44*, 3955.
[20] U. Gupta, B. S. Naidu, U. Maitra, A. Singh, S. N. Shirodkar, U. V. Waghmare, C. N. R. Rao, *APL Mater.* **2014**, *2*, 092802.
[21] B. Radisavljevic, A. Kis, *Nat. Mater.* **2013**, *12*, 815.
[22] A. Behranginia, Z. Hemmat, A. K. Majee, C. J. Foss, P. Yasaei, Z. Aksamija, A. Salehi-Khojin, *ACS Appl. Mater. Interfaces* **2018**, *10*, 24892.
[23] A. K. Majee, Z. Hemmat, C. J. Foss, A. Salehi-Khojin, Z. Aksamija, *ACS Appl. Mater. Interfaces* **2020**, *12*, 14323.
[24] Z. Hemmat, P. Yasaei, J. F. Schultz, L. Hong, L. Majidi, A. Behranginia, L. Verger, N. Jiang, M. W. Barsoum, R. F. Klie, A. Salehi-Khojin, *Adv. Funct. Mater.* **2019**, *29*, 1805693.
[25] D. H. Keum, S. Cho, J. H. Kim, D. H. Choe, H. J. Sung, M. Kan, H. Kang, J. Y. Hwang, S. W. Kim, H. Yang, K. J. Chang, Y. H. Lee, *Nat. Phys.* **2015**, *11*, 482.
[26] X. Wang, Y. Gong, G. Shi, W. L. Chow, K. Keyshar, G. Ye, R. Vajtai, J. Lou, Z. Liu, E. Ringe, B. K. Tay, P. M. Ajayan, *ACS Nano* **2014**, *8*, 5125.
[27] H. Wang, X. Huang, J. Lin, J. Cui, Y. Chen, C. Zhu, F. Liu, Q. Zeng, J. Zhou, P. Yu, X. Wang, H. He, S. H. Tsang, W. Gao, K. Suenaga, F. Ma, C. Yang, L. Lu, T. Yu, E. H. T. Teo, G. Liu, Z. Liu, *Nat. Commun.* **2017**, *8*, 394.
[28] S. J. Pennycook, D. E. Jesson, *Ultramicroscopy* **1991**, *37*, 14.
[29] P. J. Phillips, M. De Graef, L. Kovarik, A. Agrawal, W. Windl, M. J. Mills, *Ultramicroscopy* **2012**, *116*, 47.
[30] J. Ciston, C. Ophus, P. Ercius, H. Yang, R. dos Reis, C. T. Nelson, S.-L. Hsu, C. Gammer, B. V. Özdöl, Y. Deng, A. Minor, *Microsc. Microanal.* **2016**, *22*, 1412.
[31] L.-L. Wei, S.-S. Sun, K. Sun, Y. Liu, D.-F. Shao, W.-J. Lu, Y.-P. Sun, H.-F. Tian, H.-X. Yang, *Chinese Phys. Lett* **2017**, *34*, 086101.

[32] Y. Nakata, K. Sugawara, R. Shimizu, Y. Okada, P. Han, T. Hitosugi, K. Ueno, T. Sato, T. Takahashi, *NPG Asia Mater.* **2016**, *8*, e321.
[33] D. Cho, G. Gye, J. Lee, S. H. Lee, L. Wang, S. W. Cheong, H. W. Yeom, *Nat. Commun.* **2017**, *8*, 392.
[34] Y. Nakata, T. Yoshizawa, K. Sugawara, Y. Umemoto, T. Takahashi, T. Sato, *ACS Appl. Nano Mater.* **2018**, *1*, 1456.
[35] A. Zunger, S.-H. Wei, L. G. Ferreira, J. E. Bernard, *Phys. Rev. Lett.* **1990**, *65*, 353.
[36] M. Chhowalla, H. S. Shin, G. Eda, L. J. Li, K. P. Loh, H. Zhang, *Nat. Chem.* **2013**, *5*, 263.
[37] N. Rohaizad, C. C. Mayorga-Martinez, Z. Sofer, M. Pumera, *ACS Appl. Mater. Interfaces* **2017**, *9*, 40697.
[38] E. Kamil, J. Berges, G. Schönhoff, M. Rösner, M. Schüler, G. Sangiovanni, T. O. Wehling, *J. Phys. Condens. Matter* **2018**, *30*, 325601.
[39] M. Yu, D. R. Trinkle, *J. Chem. Phys, ACS Appl. Nano Mater.* **2011**, *134*, 064111.
[40] G. Henkelman, A. Arnaldsson, H. Jónsson, *Comput. Mater. Sci.* **2006**, *36*, 354.
[41] A. Allouche, *J. Comput. Chem.* **2012**, *32*, 174.
[42] W. Tang, E. Sanville, G. Henkelman, *J. Phys. Condens. Matter* **2009**, *21*, 084204.
[43] R. F. W. Bader, *Acc. Chem. Res.* **1985**, *18*, 9.
[44] T. Yanase, S. Watanabe, M. Weng, M. Wakeshima, Y. Hinatsu, T. Nagahama, T. Shimada, *Cryst. Growth Des.* **2016**, *16*, 4467.
[45] T. Gruner, D. Jang, Z. Huesges, R. Cardoso-Gil, G. H. Fecher, M. M. Koza, O. Stockert, A. P. Mackenzie, M. Brando, C. Geibel, *Nat. Phys.* **2017**, *13*, 967.
[46] Y. Yu, F. Yang, X. F. Lu, Y. J. Yan, Y. H. Cho, L. Ma, X. Niu, S. Kim, Y. W. Son, D. Feng, S. Li, S. W. Cheong, X. H. Chen, Y. Zhang, *Nat. Nanotechnol.* **2015**, *10*, 270.
[47] X. Xi, L. Zhao, Z. Wang, H. Berger, L. Forró, J. Shan, K. F. Mak, *Nat. Nanotechnol.* **2015**, *10*, 765.
[48] A. van de Walle, M. Asta, G. Ceder, *Calphad* **2002**, *26*, 539.
[49] J. P. Perdew, K. Burke, M. Ernzerhof, *Phys. Rev. Lett* **1996**, *77*, 3865.
[50] G. Kresse, J. Furthmüller, *Comput. Mater. Sci.* **1996**, *6*, 15.
[51] J. D. Pack, H. J. Monkhorst, *Phys. Rev. B* **1977**, *16*, 1748.